Three-dimensional photolithography simulator including rigorous nonplanar exposure simulation for off-axis illumination

H. Kirchauer and S. Selberherr

Institute for Microelectronics, TU Vienna, Gußhausstraße 27–29, A-1040 Vienna, Austria

ABSTRACT

Progress in today's semiconductor industry has been mainly achieved by decreasing the minimal feature size and increasing the complexity and thus the nonplanarity of the devices. Therefore lithography tools have to provide high resolution with a reasonably large depth of focus. Well-established methods to achieve both requirements are off-axis illumination techniques. As topography effects such as nonplanar electromagnetic scattering and notching are critical for line-width control, a rigorous three-dimensional exposure simulation considering both nonplanar surfaces as well as off-axis illumination is of utmost interest. We propose a rigorous method that meets the two challenges of nonplanar substrates and off-axis illumination. Our approach is based on a novel extension of the differential method to the third dimension. It is based on a Fourier expansion of the electromagnetic field in the lateral coordinates and thus belongs to the category of frequency-domain solvers. Due to the moderate computational costs nonplanar topography simulations including off-axis illumination can be performed on common engineering workstations. We will give a survey over the numerical algorithm of the differential method, describe the interface to the imaging and development module, and demonstrate the ability of the overall simulator by comparing simulation results for contact-hole printing over a dielectric and reflective substrates for various illumination apertures.

Keywords: Off-axis illumination simulation, exposure simulation, rigorous electromagnetic, vector-valued, three-dimensional, nonplanar topography, development simulation, cellular-based

1. INTRODUCTION

A rigorous *electromagnetic (EM)* field calculation becomes necessary to cope with the phenomena that determine the performance of today's semiconductor photolithography. The major reasons are that (i) the resolved lithographic feature size is on the order of or even below the actinic wavelength, (ii) the incident light is considerably oblique due to the usage of high-numerical aperture projection systems, (iii) reflection and notching effects are caused by a nonplanar topography, and (iv) the exposing light scatters inside the inhomogeneous resist. Unfortunately rigorous modeling of EM problems in photolithography simulation is particularly computation-intensive since the assumptions made throughout geometric optics as well as throughout Rayleigh's method fail as the radii of curvature cannot be neglected with respect to the disturbances caused by the discontinuity of the medium. The general problem of EM scattering from an inhomogeneous medium and/or a reflective topography has been addressed in various ways.

The first attempts were based on the finite-element method together with the boundary-element method.[1-3] However, the meshing of the simulation domain is in three-dimensions an extremely difficult task, and the bandwidth of the system matrix, and thus to a large degree also the CPU time, is determined by the number of boundary elements since the radiation boundary conditions establish tight relations between all boundary points.

An alternative method relies on the time-domain finite-difference technique. This method was successfully implemented in the lithography simulator TEMPEST at the UC Berkeley.[4-6] Problems arise from the iterative computation of the steady-state field distribution since the number of iteration cannot easily be determined as well as from the extreme computational requirements that prohibit a workstation based application in three dimensions. An advantage is its short computation time—typically 20 minutes[6]—due to the massively parallel implementation.

A totally different approach is pursued in case of frequency-domain methods. Here the EM field is represented by a superposition of some basis functions. A compromise between storage and CPU demands—typical values are 250 MB of memory and 6 hours run-time on a modern engineering workstation—is thereby realized and workstation based rigorous simulations also for three dimensions become thus feasible. If harmonic basis functions are chosen, the EM field representation refers to a Fourier expansion. Then two different discretization techniques can be

employed to the Maxwell equations. Either the partial differential equations are directly transformed to a linear algebraic system by solving repeatedly an eigenvalue problem or, alternatively, an *ordinary differential equation (ODE)* system is set up first that is then discretized resulting also in an algebraic system. The two techniques are commonly called waveguide method and differential method, respectively. The waveguide method was incorporated into the lithography simulator METROPOLE at the Carnegie Mellon University,[7-9] whereas the differential method was implemented in the two-dimensional lithography simulator iPHOTO developed at INTEL.[10] Its extension to the third dimension was developed at the Technical University of Vienna.[11-13] The differences between waveguide and differential method are of sophisticated nature and will be sketched in some detail in Sect. 2.2.

The paper is organized as follows: In Sect. 2 a survey of the three-dimensional formulation of the differential method is given. In Sect. 3 the incorporation of the field solver into the overall lithography simulator is described, whereas in Sect. 4 simulation results for resist exposure and development over nonplanar topography and off-axis illumination are presented.

2. THREE-DIMENSIONAL DIFFERENTIAL METHOD

We chose the differential method among the suitable rigorous simulation techniques for the following reasons: Meshing problems are avoided since only a simple equally spaced ortho product tensor grid is needed due to the usage of the FFT algorithm to evaluate the Fourier expansions of the EM field. Furthermore the boundary conditions are met in a natural way since the EM field outside the simulation domain can also be expressed by Fourier or Rayleigh expansions. The perhaps most important reason is the possibility to run rigorous nonplanar lithography simulation on a common engineering workstation. In the following two sections we will first give an overview of the operation principle of the differential method and then describe its performance.

2.1. Operation Principle of the Differential Method

The differential method requires a laterally periodic wafer topography. The simulation domain is one period ($a \times b \times h$) of such a periodic formation and is thus always rectangular shaped. Inside the simulation domain arbitrary inhomogeneous as well as nonplanar regions can be treated. For example, in the presented simulation results in Sect. 4 the simulation domain consists of the inhomogeneous resist and the nonplanar step. Above and below multiple planar but homogeneous material layers can be treated. In our situation we have vacuum above and a silicon substrate below (cf. Fig. 1).

The differential method itself can be divided into two stages. First, the dependence of the EM field on the lateral x- and y-coordinates is expressed by Fourier expansions. Such expansions presume a periodic EM field. For that two requirements have to be fulfilled: (i) The *incident light* is periodic, which holds since we assume a periodic mask pattern and consider only point sources located at specific positions in the source plane (cf. Sect. 3.1); (ii) The *permittivity* is periodic, too, which is true due to the specific choice of the simulation domain. Insertion of the expansions into the Maxwell equations transforms the partial differential equations into an ODE system. Once the *boundary conditions (BCs)* are determined the ODE system is solved and the obtained EM field coefficients are transformed back to the spatial domain. The mathematical formulation of this procedure reads as follows.

Since the light sources used in lithography are strictly monochromatic and only the steady-state field distribution has to be calculated, a phasor notation for the EM field vectors applies, i.e., $\mathcal{U}(\mathbf{x};t) = \mathrm{Re}\{\mathbf{U}(\mathbf{x})e^{j\omega_0 t}\}$, whereby the phasor $\mathbf{U}(\mathbf{x})$ stands vicariously for the electric and magnetic phasors, $\mathbf{E}(\mathbf{x})$ and $\mathbf{H}(\mathbf{x})$, respectively, $\omega_0 = 2\pi/\sqrt{\varepsilon_0\mu_0}\lambda_0$ is the angular frequency, and λ_0 denotes the actinic wavelength. The phasors $\mathbf{E}(\mathbf{x})$ and $\mathbf{H}(\mathbf{x})$ obey the time-harmonic version of the Maxwell equations,[14]

$$\mathrm{curl}\,\mathbf{H}(\mathbf{x}) = -j\omega\varepsilon_0\varepsilon(\mathbf{x})\mathbf{E}(\mathbf{x}) \qquad \text{and} \qquad \mathrm{curl}\,\mathbf{E}(\mathbf{x}) = j\omega\mu_0\mathbf{H}(\mathbf{x}). \tag{1}$$

The two EM phasors $\mathbf{U}(\mathbf{x})$ as well as the inhomogeneous permittivity* $\varepsilon(\mathbf{x})$ are now expanded like

$$\mathbf{U}(\mathbf{x}) = \sum_{n,m} \mathbf{U}_{nm}(z)e^{j2\pi(nx/a+my/b)} \qquad \text{and} \qquad \varepsilon(\mathbf{x}) = \sum_{n,m} \varepsilon_{nm}(z)e^{j2\pi(nx/a+my/b)}. \tag{2}$$

---

*In addition to the permittivity also its reciprocal $\chi(\mathbf{x}) = \varepsilon^{-1}(\mathbf{x})$ has to be expanded into Fourier series. For details see Ref. 13.

Insertion of Eq. (2) into Eq. (1) transforms the Maxwell equations into an ODE system that can be written in compact matrix-vector notation as

$$\frac{d}{dz}\mathbf{u}(z) = \underline{\mathbf{H}}(z)\mathbf{u}(z) \qquad \text{with} \qquad \underline{\mathbf{H}}(z) = \begin{bmatrix} \underline{\mathbf{0}} & \underline{\mathbf{R}}(z) \\ \underline{\mathbf{G}}(z) & \underline{\mathbf{0}} \end{bmatrix}. \tag{3}$$

The complex-valued vector $\mathbf{u}(z)$ comprises the Fourier coefficients of the lateral field components only, as the vertical components can be analytically expressed by the lateral ones. This fact is a big advantage of frequency methods—it also applies for the waveguide method[9]—since the number of unknown quantities for each harmonic frequency (nm) is reduced from 6 to 4. The system matrix $\underline{\mathbf{H}}(z)$ contains the Fourier coefficients of the permittivity. Its shape reflects the fundamental structure of the Maxwell equations since the derivative of the electric phasor depends only on the magnetic phasor and vice versa. The potential run-time speedup is large due the analytical elimination of the vertical components and the special structure of the system matrix. To solve the infinitely dimensional ODE system numerically, the Fourier expansions are truncated, i.e., only coefficients $U_{nm}(z)$ symmetrically centered around the principal incident ray $n = m = 0$ are considered. The thereby entailed approximations will be discussed in the next section. The dimension of the resulting *finite-dimensional* ODE system equals

$$N_{\text{ODE}} = 4 \times (2N_x + 1) \times (2N_y + 1) \approx 16 \times N_x \times N_y, \tag{4}$$

whereby N_x and N_y are the truncation frequencies in x- and y-direction, respectively. The factor four is due to the four lateral field components, the truncation frequencies have to be counted twice to account for "positive" and "negative" harmonics, and the additive one results from the zeroth-order harmonic.

The BCs for the ODE system are obtained by matching the Fourier expansions valid inside the simulation domain (cf. Eq. (2)) to the Rayleigh expansions valid above and below the simulation domain (cf. Eq. (8)). The mathematical formulation of a Rayleigh expansion is that of a Fourier expansion with vertically known dependence of the coefficients and has the physical interpretation of a superposition of plane waves. Hence, the BCs follow from a simple comparison of the Fourier coefficients. It can be shown (see Ref. 13) that half of the required N_{ODE} BCs are located at the resist/air interface at $z = 0$, and the other half at the resist/substrate interface at $z = h$. Using again a matrix-vector notation they take the form

$$\underline{\mathbf{B}}_0\mathbf{u}(0) = \mathbf{a} \qquad \text{and} \qquad \underline{\mathbf{B}}_h\mathbf{u}(h) = \mathbf{0}. \tag{5}$$

To clarify the notation we list the dimensions of the involved quantities: The vector $\mathbf{u}(z)$ containing the N_{ODE} unknown vertically dependent Fourier coefficient belongs to $\mathbf{u}(z) \in \mathbb{C}^{N_{\text{ODE}}}$, the excitation vectors $\mathbf{a}$ and $\mathbf{0}$ comprising the incident field coefficients at the two boundary points are elements of $\mathbf{a}, \mathbf{0} \in \mathbb{C}^{N_{\text{ODE}}/2}$, and the two boundary matrices $\underline{\mathbf{B}}_0$ and $\underline{\mathbf{B}}_h$ are of dimension $\underline{\mathbf{B}}_0, \underline{\mathbf{B}}_h \in \mathbb{C}^{N_{\text{ODE}} \times N_{\text{ODE}}/2}$. Note that the excitation vector at the lower interface at $z = h$ equals the zero-vector $\mathbf{0}$ since no light is incident at the bottom of the simulation domain. This situation is only valid if one homogeneous layer, i.e., the substrate, is situated below the simulation domain. Otherwise a stack of homogeneous layers forms a stratified medium that can be treated analytically. A detailed description of this different situation can be found in Ref. 15.

The final step is the numerical solution of the ODE system subject to the BCs, whereby Eqs. (3) and (5) constitute a two-point boundary value problem. We adapted the shooting method[16] since it can be implemented in a very memory saving way. The main ideas of the algorithm are outlined in the following, for a throughout discussion see Ref. 15. Firstly, the two boundary points $z = 0$ and $z = h$ are related by recursively evaluating a relation like[†] $\mathbf{u}(z_{j+1}) = \underline{\mathbf{S}}_j\mathbf{u}_j(z)$ between two adjacent mesh points z_j and z_{j+1}, i.e.,

$$\mathbf{u}(z_{j+1}) = \underline{\mathbf{S}}_j\mathbf{u}_j(z) \qquad \Longrightarrow \qquad \mathbf{u}(h) = \left(\prod_{j=1}^{N_z}\underline{\mathbf{S}}_j\right)\mathbf{u}(0) = \underline{\mathbf{S}}\mathbf{u}(0). \tag{6}$$

Combining Eqs. (5) and (6) yields an algebraic system for the initial values at one boundary point, e.g., at $z = 0$,

$$\begin{bmatrix} \underline{\mathbf{B}}_0 \\ \underline{\mathbf{B}}_h\underline{\mathbf{S}} \end{bmatrix}\mathbf{u}(0) = \begin{bmatrix} \mathbf{a} \\ \mathbf{0} \end{bmatrix}. \tag{7}$$

[†]Such a relation can easily be obtained by applying an explicit discretization scheme to (3). However, due to numerical instabilities more advanced techniques like multiple shooting, decoupling, and stabilized marching techniques have to be applied.[16]

This algebraic system is solved for $\mathbf{u}(0)$. Since the vector of unknowns is now known at the boundary point $z = 0$, the originally boundary value problem is transformed to an initial value problem that can be simply integrated to obtain $\mathbf{u}(z_j)$ at any desired vertical discretization point z_j. The vector $\mathbf{u}(z_j)$ comprises the Fourier coefficients $\mathbf{U}_{nm}(z_j)$ of the EM field phasors and the spatial field distribution is obtained by transforming them according to Eq. (2).

2.2. Performance of the Differential Method

The proposed algorithm has the big advantage that the vertical mesh size N_z does not influence the storage consumption since the recursion matrices $\underline{S}_j$ in Eq. (6) do not have to be stored individually. The memory usage is thus only determined by the rank N_{ODE} of the ODE system (cf. Eq. (4)). It is of order $\mathcal{O}(N_{\text{ODE}}^2) \approx 256 \times \mathcal{O}(N_x^2 \times N_y^2)$. Typical values for the truncation frequencies are $N_x = N_y = 16$. 33 Fourier modes are then considered in each lateral direction and approximately 300 MB of memory are required, whereby 16 Bytes are assumed to store a complex number with double precision. These requirements are in accordance with the waveguide model[9] and lie dramatically below the time-domain finite-difference approach.[4] The numerical costs are mainly determined by the evaluation of the recursion formula in Eq. (6) and by the solution of the algebraic equation system in Eq. (7). Both operation are of order $\mathcal{O}(N_{\text{ODE}}^3)$. Hence, the total run-time grows for N_z vertical discretization points with $\mathcal{O}(N_z \times N_{\text{ODE}}^3)$ and lies typically under a few hours on a DEC-600/333 workstation.

In the preceding discussion of the storage consumption it was shown that the memory grows with the second order of the number N_{ODE} of considered Fourier coefficients. Hence, the truncations frequencies N_x and N_y determining N_{ODE} (cf. Eq. (4)) shall be chosen as small as possible. The following considerations explain the tradeoff between storage costs and simulation accuracy. The truncation of the Fourier expansions of the EM field entails two important implications: (i) A low-pass filtering of the *field*, and (ii) a low-pass filtering of the *geometry*. The first one is obvious, the second, however, is more involved. This stems from the fact that the neglected field coefficients are coupled to the considered ones due to the fully occupied matrices $\underline{R}(z)$ and $\underline{G}(z)$ in Eq. (3). Hence, the inhomogeneity is treated as it would be that smooth that only negligible coupling from and to higher order harmonics occur. This assumption is of course only true for small variations of the refractive index or, similarly, for a smooth topography. In both cases the permittivity is a low-pass function. For the special situation of a homogeneous medium no coupling occurs at all and no approximation errors are caused by the truncation. However, this situation is of no interest and can be treated analytically anyway. Numerical investigations show that above a certain truncation level the solution converges and additional Fourier coefficients do not alter the results significantly. On the contrary, such high-order harmonics aggravate the condition of the ODE system since they refer to highly damped or evanescent modes in vertical direction. The spectral range of the final linear equation system for the initial values (cf. Eq. (3)) can be shown to fall of above a certain truncation level.[15] Resembling problems occur if the materials are too absorptive, but then even low-order harmonics are strongly damped.

Similar limitations apply for the waveguide model, since they are implicitly contained in any frequency domain method. However, exactly in the treatment of such stability problems the advantage of the differential method over the waveguide method lies. To explain this a few notes on the waveguide method are necessary. The waveguide method divides the simulation domain into thin layers with a vertically constant refractive index. Within one layer an eigenvalue problem is solved. By matching recursively adjacent layers a linear algebraic system is established. This procedure refers to the vertical discretization of the ODE system employed throughout the differential method (cf. Eq. (6)). Hence we see that the waveguide equals the zeroth-order discretization of the differential method since an ODE system with constant coefficients can be reduced to an eigenvalue problem. Consequently, the discretization order of the differential method is implicitly higher than that of the waveguide method. It can be chosen arbitrarily and numerical problems can thus be reduced by simply increasing it. Computationally efficient algorithms exist to solve "stiff" two-point boundary value problems[16] that assure good convergence in even stronger absorptive media. This is an important advantage of the differential method over the waveguide method. A similar relation is known between the modal and the coupled-wave approach[17] that are based on the same theories as the waveguide and the differential method, respectively, and are well-known in the study of diffraction gratings.

3. OVERALL SIMULATOR STRUCTURE

In this section we describe how the differential method is incorporated into the overall photolithography simulator. The simulator consists of three basic modules, whereby each of them accounts for one of the fundamental phases of the lithography simulation,[18] namely imaging, exposure, and development.

3.1. Aerial Image Calculation

Our aerial image simulator is based on the vector-valued extension[10] of the scalar theory of Fourier optics.[19] The mask-pattern is thereby assumed to be laterally periodic and the photomask is infinitesimally thin with ideal transitions of the transmission characteristic. To account for general illumination forms like circular or quadrupole illumination the distributed light source is discretized into mutually independent coherent source points Q_{pq}. This approach is commonly referred to as Abbe's method.[14] The resulting image incident on top of the wafer due to one coherent point source is expressed by a superposition of homogeneous plane waves, i.e., by a Rayleigh expansion. For a numerically efficient exposure simulation is is necessary to restrict the location of the source points to an equally spaced ortho product tensor grid so that all contributions are periodic. A generalization of this procedure to a finer grid resulting in a quasi-periodic incident field is possible but is beyond the scope of this paper. The spacing between the individual source points Q_{pq} is chosen in such a way that the lateral wavevector components $s_{x,p}$ and $s_{y,q}$ of the waves incident on the mask equal an integer multiple of the sampling frequencies $2\pi/a$ and $2\pi/b$ in the Fourier domain, i.e., $s_{x,p} = 2\pi p/a$ and $s_{y,q} = 2\pi q/b$, whereby a and b are the periods of the photomask[‡] and, simultaneously, the lateral extensions of the simulation domain required by the differential method. Examples of the wavevector sampling for various apertures are shown in Fig. 2. The EM field that is excited by one coherent source point Q_{pq} and is incident on the mask can now be expressed by[10]

$$\mathbf{U}_i^{pq}(\mathbf{x}) = \sum_{nm} \mathbf{U}_{i,nm}^{pq} e^{j2\pi(nx/a + my/b)} e^{j2\pi\sqrt{1-(nx/a)^2-(my/b)^2}z/\lambda_0}, \tag{8}$$

whereby $\mathbf{U}_i^{pq}(\mathbf{x})$ stands vicariously for the electric $\mathbf{E}_i^{pq}(\mathbf{x})$ and magnetic $\mathbf{H}_i^{pq}(\mathbf{x})$ field vector. The amplitudes of the electric diffraction orders follow from the vector-valued diffraction theory[10]

$$\mathbf{E}_{i,nm}^{pq} = A_{pq} T_{n-p,m-q} \mathbf{P}(n,m:p,q) F(n,m) e^{j\Phi(n,m)}, \tag{9}$$

and the magnetic ones can be calculated from $\mathbf{H}_{i,nm}^{pq} = \lambda_0/2\pi \sqrt{\varepsilon_0/\mu_0}\, \mathbf{k}_{nm} \times \mathbf{E}_{i,nm}^{pq}$. In Eq. (9) A_{pq} refers to the source point amplitude that depends on the illumination intensity and the discretization area w_{pq} inside the aperture (cf. Fig. 2), T_{nm} are the Fourier coefficients of the mask transmission function, $\mathbf{P}(n,m:p,q)$ is the vector-valued pupil function, $F(n,m)$ stands for a possible in-lens filter function, and $\Phi(n,m)$ is the aberration function of the projection lens. Expressions for the vector-valued pupil function $\mathbf{P}(n,m:p,q)$ can be found in Ref. 10. The aerial image, i.e., the two-dimensional light intensity incident on top of the photoresist is given by the incoherent superposition of the vertical components of the Poynting vectors of all source point contributions. The amplitudes of the electric diffraction orders $\mathbf{E}_{i,nm}^{pq}$ given in Eq. (9) are the input to the exposure module described next.

3.2. Exposure Simulation

The chemical state of the photoresist during exposure is characterized by the concentration of the *photoactive compound (PAC)* $M(\mathbf{x};t)$ in case of conventional DQN resists[20] and by the concentration of the *photoacid generator (PAG)* $G(\mathbf{x};t)$ in case of chemically amplified resists.[21] In both situations the interaction of the resist with the exposing light can be described by a first-order dissolution law[20,21]

$$\frac{\partial \gamma(\mathbf{x};t)}{\partial t} = -CI(\mathbf{x};t)\gamma(\mathbf{x};t), \tag{10}$$

whereby the concentration $\gamma(\mathbf{x};t)$ refers either to the PAC or the PAG and $I(\mathbf{x};t)$ denotes the absorbed light intensity. Equation (10) describes the fundamental property of a photoresist: The exposing light $I(\mathbf{x};t)$ is stored in a latent bulk image $\gamma(\mathbf{x};t)$. However, the physical processes governing the conversion of the photosensitive component are of different nature for the two considered resist systems. DQN resists exhibit a so-called bleaching phenomenon, i.e., the resist becomes more transparent during exposure. This means that the optical properties depend on the concentration of the PAC. Dill's 'ABC'-model[20] postulates a simple relation between the refractive index $n(\mathbf{x};t)$ of the resist and the PAC $M(\mathbf{x};t)$, $n(\mathbf{x};t) = n_0 + j\lambda_0/4\pi(AM(\mathbf{x};t) + B)$. In case of chemically amplified resists the bleaching phenomenon usually does not occur, but the PAG has to be thermally activated after exposure. Thereby the generated acid acts as a catalyzer and the latent image $G(\mathbf{x};t)$ is chemically amplified. Such a post-exposure

---

[‡]Here we assume a magnification M of one. Otherwise the sampling frequencies $s_{x,p}$ and $s_{y,q}$ have to be multiplied by M or, equivalently, the mask transmission function has to be scaled by M.

bake step is also often applied to DQN resists. Here they have the purpose to smooth variations in the latent PAC image $M(\mathbf{x}; t)$ that are caused by standing waves.[22] Disregarding any further chemical details we proceed with the description of the exposure module.

By applying a quasi-static approximation to the dissolution law Eq. (10) is explicitly discretized with respect to time

$$\gamma(\mathbf{x}; t_{k+1}) = \gamma(\mathbf{x}; t_k)e^{-CI(\mathbf{x}; t_k)(t_{k+1} - t_k)}.$$

This is justified since the dissolution rate is always negligible in comparison to the optical frequency. For the same reason a steady-state field distribution can be assumed within one time-step $t_k \le t < t_k$. Therefore the EM field is time-harmonic and obeys the Maxwell equations in the form of Eq. (1), whereby the permittivity $\varepsilon_k(\mathbf{x})$ is related to the refractive index by Maxwell's law[14] $\varepsilon_k(\mathbf{x}) = n(\mathbf{x}; t_k)$. The absorbed light intensity $I(\mathbf{x}; t_k)$ can simply be calculated from the electric field distribution $I(\mathbf{x}; t_k) = 0.5n_o\sqrt{\varepsilon_0/\mu_0}\|\mathbf{E}_k(\mathbf{x}\|^2$. The crucial point of the exposure module is the numerical solution of the Maxwell equations. We use the differential method as described in Sect. 2, whereby special care has to be taken in case of off-axis or partially coherent illumination.

As outlined in the preceding section the amplitudes of the electric diffraction orders $\mathbf{E}_{i,nm}^{pq}$ given in Eq. (9) are the input to the exposure module. Assuming N_s source points Q_{pq} the Maxwell equations of Eq. (1) have to be solved for N_s different BCs. With the proposed formulation of the differential method this can be done in a very efficient way. For each source point Q_{pq} we get an own excitation vector $\mathbf{a}^{pq}$ in Eq. (5). As all contributions are periodic (cf. Eq. (8)) the system matrix $\underline{\mathbf{H}}(z)$ and the two boundary matrices $\underline{\mathbf{B}}_0$ and $\underline{\mathbf{B}}_h$ are *independent* of (pq). Hence, the vertical discretization, i.e., the recursion in Eq. (7), has to be evaluated just *once*. The final algebraic system can be *simultaneously* solved for all N_s right-hand sides, i.e.,

$$\begin{bmatrix} \underline{\mathbf{B}}_0 \\ \underline{\mathbf{B}}_h \underline{\mathbf{S}} \end{bmatrix} \underline{\mathbf{U}}(0) = \begin{bmatrix} \underline{\mathbf{A}} \\ \underline{\mathbf{0}} \end{bmatrix} \tag{11}$$

with

$$\underline{\mathbf{U}}(0) = \begin{bmatrix} \cdots & \mathbf{u}^{pq}(0) & \cdots \end{bmatrix} \qquad \text{and} \qquad \underline{\mathbf{A}} = \begin{bmatrix} \cdots & \mathbf{a}^{pq} & \cdots \end{bmatrix}.$$

The final linear system of Eq. (11) incorporating the N_s right-hand sides can be efficiently solved by employing a LU-factorization[23] and the therefrom calculated light intensities are incoherently superposed. The extra effort due the off-axis apertures is of one order lower than the overall numerical costs and thus negligible. No further modifications of the proposed implementation of the differential method are thus required. This is a big advantage since in other techniques the Maxwell equations have to solved separately for the N_s BCs and the computationally costs grow proportionally to N_s.[24]

Finally, we want to point out that the quasi-static approximation transforms the originally nonlinear problem to a series of inhomogeneous but linear problems. Without the bleaching reaction, i.e., the optical properties do not depend on $\gamma(\mathbf{x}; t)$, we have to consider only one time step. This situation will usually apply for chemically amplified resist systems. Furthermore, we do not treat the required or optional post-exposure bake step in any greater depth as the main concern of the paper is the presentation of the rigorous EM field calculation under aperture illumination. A simple first order model is a diffusion simulation with a constant diffusion coefficient[22] that refers to a convolution of $\gamma(\mathbf{x}; t)$ with a Gaussian.

3.3. Development Simulation

The development of the photoresist is modeled as a surface-controlled etching reaction.[25] Among the models available in the open literature we choose Kim's 'R'-model to relate the chemical state after the exposure simulation to a spatially inhomogeneous development rate.[26] This development rate is stored on a ortho tensor product grid, since the above discussed differential method requires a laterally uniform spaced grid to apply the numerically highly efficient two-dimensional FFT algorithm. For the simulation of the time-evolution of the development front we adapted the recently proposed cellular-based topography simulator[27] to read the development rate from the grid. The basic idea behind this surface advancement algorithm is to apply a structuring element along the exposed surface that removes successively photoresist cells of the underlying cellular geometry representation. Within the scope of lithography simulation the shape of the structuring element depends on the precalculated development rate multiplied by the chosen time step. As the development rate exhibits a strong dependence on the spatial coordinates, e.g., due to standing waves or notching effects during photoresist exposure, a sufficiently high number of cells has to be chosen to resolve these variations.

For example, in case of standing waves over a planar reflective substrate we know that the distance between the maxima and minima of the absorbed light intensity and therefore also of the development rate is $\lambda_{Resist}/4$, which yields approximately 37 nm for DUV illumination at a wavelength of $\lambda_0 = 248$ nm and a refractive index of 1.65 of the photoresist. For an accurate movement of the development front this significant distance should be resolved by at least 10 cells.[27] Hence a cell density of 300 cells/μm is required. The applicability of the structuring element algorithm for this cellular geometry resolution has been demonstrated in Ref. 27.

4. SIMULATION RESULTS

To demonstrate the capability of our approach we simulated 248 nm DUV contact hole printing over dielectric and reflective substrate topography with various aperture systems. Additionally, we investigated defocus effects since the advantage of off-axis systems lies in a greater depth of focus.

In all cases the simulation domain was 1.0 μm × 1.0 μm × 0.7 μm large and the substrate material was silicon with a refractive index of $n_{Si} = 1.68 + j3.58$. The step was centered in the middle of the simulation domain, the height was 0.25 μm and the slope was 45°. The step material was either dielectric oxide with a refractive index of $n_{SiO_2} = 1.508$ or reflective a-silicon with a refractive index of $n_{a\text{-}Si} = 1.69 + j2.76$. A non-bleaching resist was chosen with a refractive index of $n_{Resist} = 1.65 + j0.02$. The mask was located in the center of the geometry, i.e., exactly above the slope, and the mask-opening was 0.25 μm × 0.25 μm wide. A sketch of the investigated configuration is shown in Fig. 1.
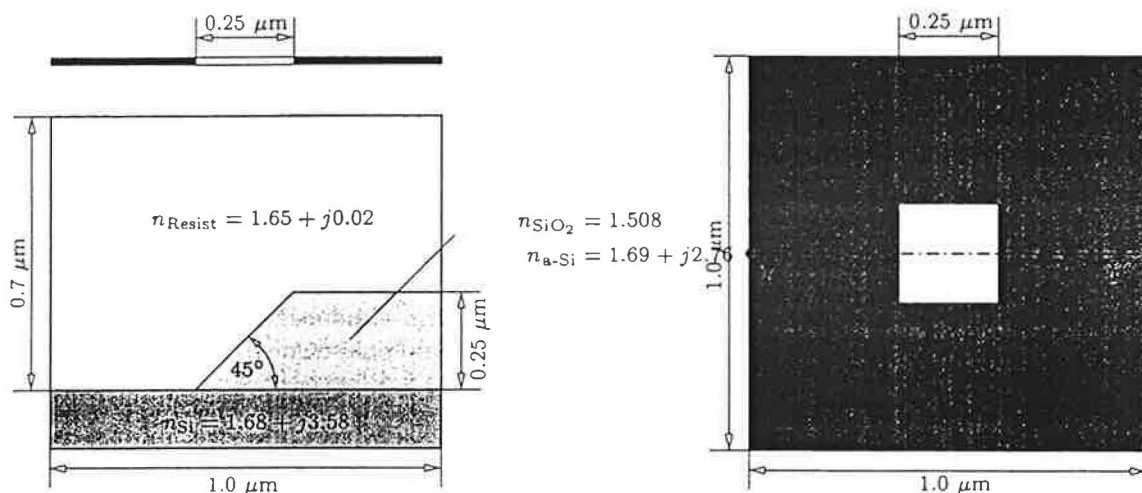

Figure 1. Schematic of the simulation domain: Cut along $\overline{YY'}$ (left) and top-view (right).

For the simulation 51 Fourier modes in x-direction and 21 in y-direction corresponding to cut-off frequencies of $N_x = 25$ and $N_y = 10$, respectively, were used to represent the EM field. The differential method thus consumed approximately 300 MB. The number N_z of discretization points were in the dielectric case 50 and in the reflective case 75 since the stronger absorption in a-silicon has to be resolved properly. The run-time ranged between 4 to 5 hours on a DEC-600/333 workstation depending on the step material. The development simulation was performed with a cell density of 300 cells/μm. The memory usage was 20 MB assuming 1 Byte per cell and the run time was 25 minutes.

We investigated three different illumination configurations with a fixed numerical aperture of $NA = 0.5$, namely coherent, partially coherent or circular with $\sigma = 0.8$, and quadrupole with $\sigma = 0.1$ and $X = Y = 0.7$. The number and location of the source points are illustrated in the discretized wavevector diagram of Fig. 2. In Fig. 3 and 4 we show the simulated PAC concentrations after an exposure of dose 120 mJ/cm^2 obtained for the dielectric and reflective topography, respectively. The absorption parameter of the resist was thereby set to $C = 0.013$ cm^2/mJ, and the Kim-parameters were taken from Table IV of Ref. 26: $R_1 = 0.25$ μm/s, $R_2 = 0.0005$ μm/s, $R_3 = 7.4$. The simulations were performed with ideal focus as well as with a defocus of 1 μm above the resist surface. The developed resist profiles resulting from the shown PAC concentrations are presented in Fig. 5 and 6. The development time was chosen so that in all cases the full contact hole was opened.
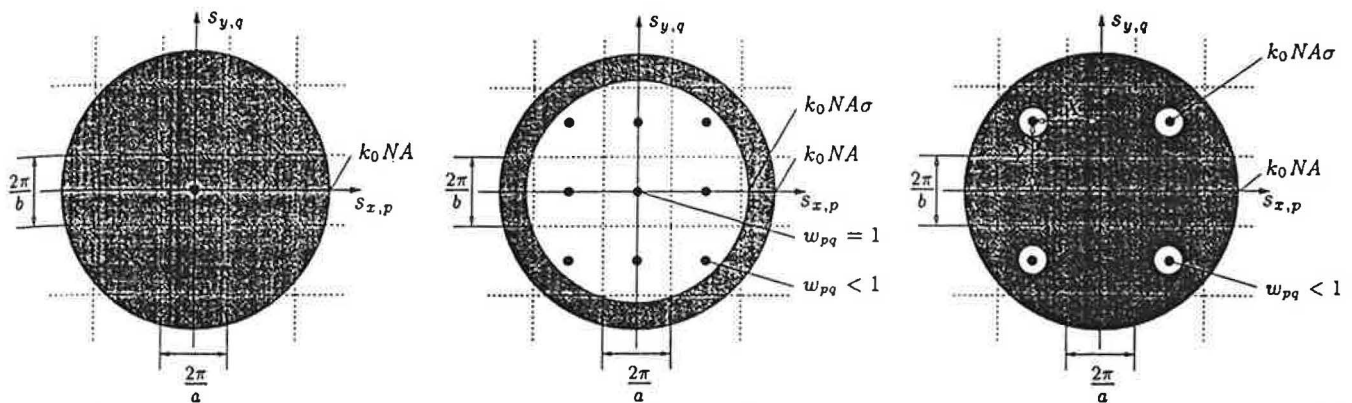
Figure 2. Source points in the discretized wavevector diagram (left: coherent, middle: circular, right: quadrupole).

A comparison of the simulation results exhibits a stronger impact of the nonplanar topography on the latent bulk image and developed resist profile in case of the reflective step than in case of the dielectric step. The standing waves caused by the abrupt change of the refractive index along the material interfaces are in both cases distorted due the nonplanarity. In case of a planar substrate the contours are ideally oval[12,13] since the optical thickness is constant across the whole simulation area. For a nonplanar topography the optical thickness varies which causes the distortion. This situation is less pronounced for the oxide since the real parts of the refractive indices of the oxide and the resist, $\mathrm{Re}\{n_{SiO_2}\} = 1.508$ and $\mathrm{Re}\{n_{Resist}\} = 1.65$, respectively, are almost matched and no reflection occurs at the dielectric, i.e., $\mathrm{Im}\{n_{SiO_2}\} = 0.0$. In case of a-silicon the conductivity, i.e., the non-vanishing imaginary part of the refractive index $\mathrm{Im}\{n_{a\text{-}Si}\} = 2.76$, forces a minimum node in the EM field distribution along the step surface which results in a maximum of the PAC concentration within the exposed resist and thus in a minimum of the development rate. Additionally, some fraction of the absorbed light intensity is scattered into nominally unexposed regions of the resist opposite the step. This can be clearly seen in the developed resist profiles. For the same reasons as before this notching effect is more distinct for the reflective topography than for the dielectric.

Regarding the various illumination forms it can be seen that the circular and quadrupole aperture perform better than the coherent one in the defocus situation. The resolution, however, is for the coherent source the best. The difference between circular and quadrupole aperture is small. This is most likely caused by the small number of considered source points (nine and four as illustrated in Fig. 2). To circumvent such inaccuracies a finer grid is necessary for the discretization of the light source into incoherent points. However, the full benefits of the proposed implementation of the differential method would be lost as the incident field would consist of quasi-periodic contributions in addition to the periodic ones of Eq. (9). Such multiple sets of quasi-periodic modes require individual reclusion matrices $\underline{S}$ in Eq. (11). But similar to the periodic modes also quasi-periodic modes with an offset equal to the fundamental frequencies $2\pi/a$ and $2\pi/b$ can be grouped together. Hence, even in case of a finer grid the numerical costs do not grow proportional to the number of point sources but proportional to the number of quasi-periodic groups. This is still a big performance gain of the differential method in comparison to other techniques.

5. CONCLUSIONS

The three-dimensional formulation of the differential method is presented and it is shown that the approach is extremely efficient to rigorously calculate the EM field over a nonplanar topography under advanced aperture illumination. The method is implemented into a computer program running on common engineering workstations. It is embedded in the exposure module of an overall three-dimensional rigorous nonplanar photolithography simulator. The interface to the two other parts, namely the vector-valued aerial image calculation and the development/etching module, is described. The capability of the simulator is demonstrated by showing simulation results of contact hole printing over dielectric and reflective substrate topography with various aperture systems.

ACKNOWLEDGMENTS

REFERENCES

1. T. Matsuzawa, A. Moniwa, N. Hasegawa, and H. Sunami, "Two-dimensional simulation of photolithography on reflective stepped substrate," *IEEE Trans. Computer-Aided Design* **CAD-6**, pp. 446–451, 1987.

2. H. P. Urbach and D. A. Bernard, "Modeling latent-image formation in photolithography, using the Helmholtz equation," *J.Opt.Soc.Am.* **A6**, pp. 1343–1356, 1989.

3. E. Barouch and B. Bradie, "Comprehensive 3-d notching simulator with non-planar substrates," in *Optical/Laser Microlithography III, Proc. SPIE* **1264**, pp. 334–342, 1990.

4. R. Guerrieri, K. H. Tadros, J. Gamelin, and A. R. Neureuther, "Massively parallel algorithms for scattering in optical lithography," *IEEE Trans. Computer-Aided Design* **10**, pp. 1091–1100, 1991.

5. A. K. Wong, R. Guerrieri, and A. R. Neureuther, "Massively parallel electromagnetic simulation for photolithographic applications," *IEEE Trans. Computer-Aided Design* **14**, pp. 1231–1240, 1995.

6. A. K. Wong and A. R. Neureuther, "Rigorous three-dimensional time-domain finite-difference electromagnetic simulation for photolithographic applications," *IEEE Trans. Semiconductor Manufacturing* **8**, pp. 419–431, 1995.

7. C. M. Yuan, "Efficient light scattering modeling for alignment, metrology, and resist exposure in photolithography," *IEEE Trans. Electron Devices* **39**, pp. 1588–1598, 1992.

8. H. Tanabe, "Modeling of optical images in resists by vector potentials," in *Optical/Laser Microlithography V, Proc. SPIE* **1674**, pp. 637–649, 1992.

9. K. D. Lucas, H. Tanabe, and A. J. Strojwas, "Efficient and rigorous three-dimensional model for optical lithography simulation," *J.Opt.Soc.Am.* **A13**, pp. 2187–2199, 1996.

10. M. S. C. Yeung, "Modeling high numerical aperture optical lithography," in *Optical/Laser Microlithography, Proc. SPIE* **922**, pp. 149–167, 1988.

11. H. Kirchauer and S. Selberherr, "Three-dimensional photoresist exposure and development simulation," in *Proc.SISPAD'96—1996 International Conference on Simulation of Semiconductor Processes and Devices*, pp. 99–100, IEEE Cat.No. 96TH8095, 1996.

12. H. Kirchauer and S. Selberherr, "Three-dimensional photolithography simulation," *IEEE Trans. Semiconductor Technology Modeling and Simulation*, http://www.ieee.org/journal/tcad/accepted/, No. 6, 1997.

13. H. Kirchauer and S. Selberherr, "Rigorous three-dimensional photoresist exposure and development simulation over nonplanar topography," *accepted for publication in IEEE Trans. Computer-Aided Design*, November 1997.

14. M. Born and E. Wolf, *Principles of Optics*, Pergamon Press, Oxford, England, 6th ed., 1993.

15. H. Kirchauer, *Photolithography Simulation*. PhD thesis, TU Vienna, Institute for Microelectronics, *in preparation* (March 1998).

16. U. M. Ascher, R. M. M. Mattheij, and R. D. Russell, *Numerical Solution of Boundary Value Problems for Ordinary Differential Equations*, Classics in Applied Mathematics Vol. 13, SIAM, Philadelphia, 1995.

17. R. Magnusson and T. K. Gaylord, "Equivalence of multiwave coupled-wave theory and modal theory of periodic-media diffraction," *J.Opt.Soc.* **A68**, pp. 1777–1779, 1978.

18. K. K. H. Toh and A. R. Neureuther, "Three-dimensional simulation of optical lithography," in *Optical/Laser Microlithography IV, Proc. SPIE* **1463**, pp. 356–367, 1991.

19. J. W. Goodman, *Introduction to Fourier Optics*, McGraw-Hill, New York, 1968.

20. F. H. Dill, W. P. Hornberger, P. S. Hauge, and J. M. Shaw, "Characterization of positive photoresist," *IEEE Trans. Electron Devices* **ED-22**, pp. 445–452, 1975.

21. D. Seligson, S. Das, H. Gaw, and P. Pianetta, "Process control with chemical amplification resists using deep ultraviolet and X-ray radiation," *J. Vac. Sci. Technol.* **B6**, pp. 2303–2307, 1988.

22. E. J. Walker, "Reduction of photoresist standing-wave effects by post-exposure bake," *IEEE Trans. Electron Devices* **ED-22**, pp. 464–466, 1975.

23. G. H. Golub and C. F. V. Loan, *Matrix Computations*, John Hopkins University Press, Baltimore, 2nd ed., 1989.

24. R. J. Socha and A. R. Neureuther, "Propagation effects of partial coherence in optical lithography," *J. Vac. Sci. Technol.* **B14**, pp. 3724–3729, 1996.

25. F. H. Dill, "Optical lithography," *IEEE Trans. Electron Devices* **ED-22**, pp. 440–444, 1975.

26. D. J. Kim, W. G. Oldham, and A. R. Neureuther, "Development of positive photoresist," *IEEE Trans. Electron Devices* **ED-31**, pp. 1730–1736, 1984.

27. E. Strasser and S. Selberherr, "Algorithms and models for cellular based topography simulation," *IEEE Trans. Computer-Aided Design* **14**, pp. 1104–1114, 1995.
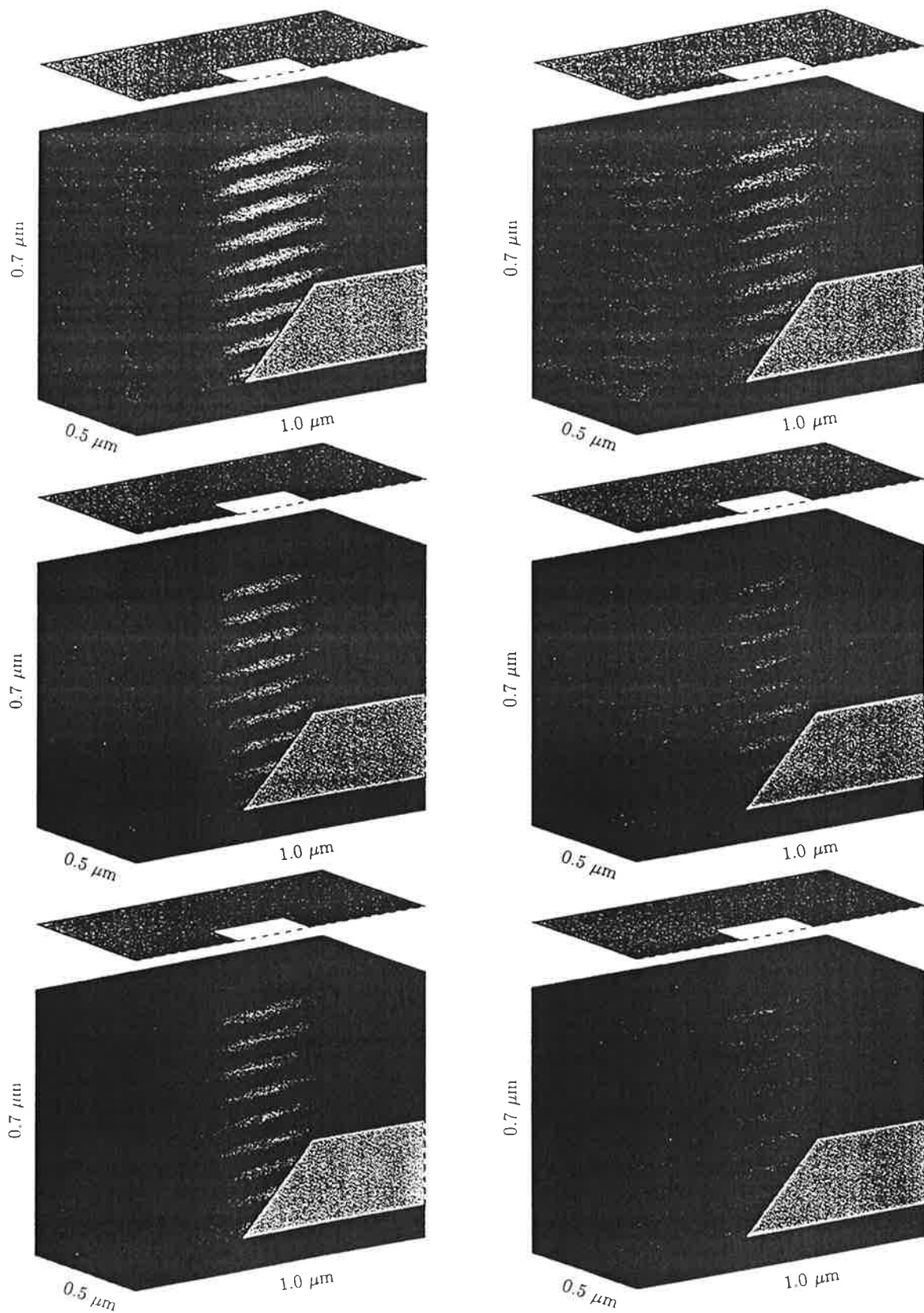
Figure 3. PAC concentration after exposure over a dielectric oxide step (left: best focus, right: 1 μm defocus above; top: coherent, middle: circular, bottom: quadrupole).
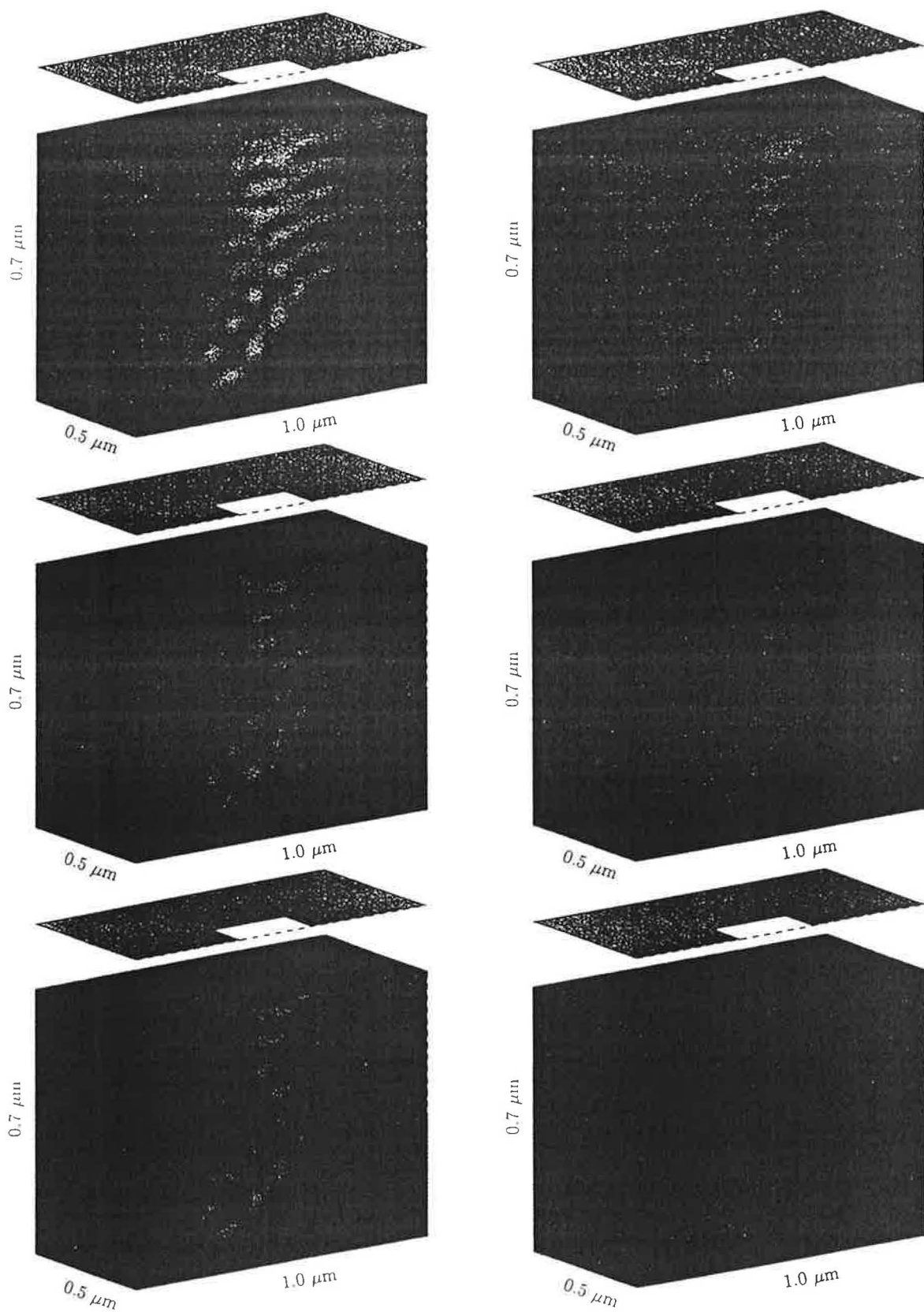
Figure 4. PAC concentration after exposure over a reflective a-silicon step (left: best focus, right: 1 μm defocus above; top: coherent, middle: circular, bottom: quadrupole).
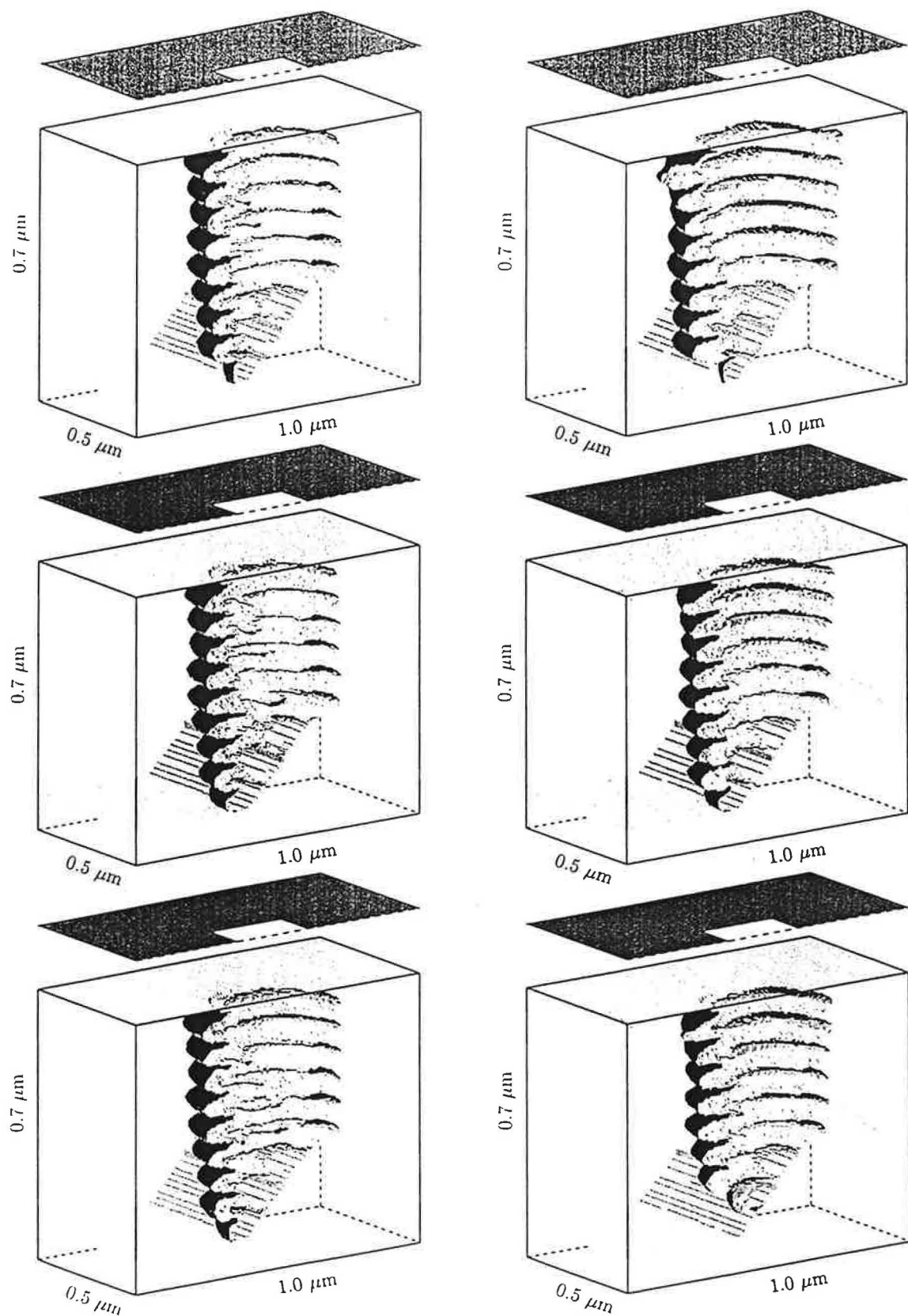
Figure 5. Resist profiles after development over a dielectric oxide step (left: best focus, right: 1 μm defocus above; top: coherent, middle: circular, bottom: quadrupole).
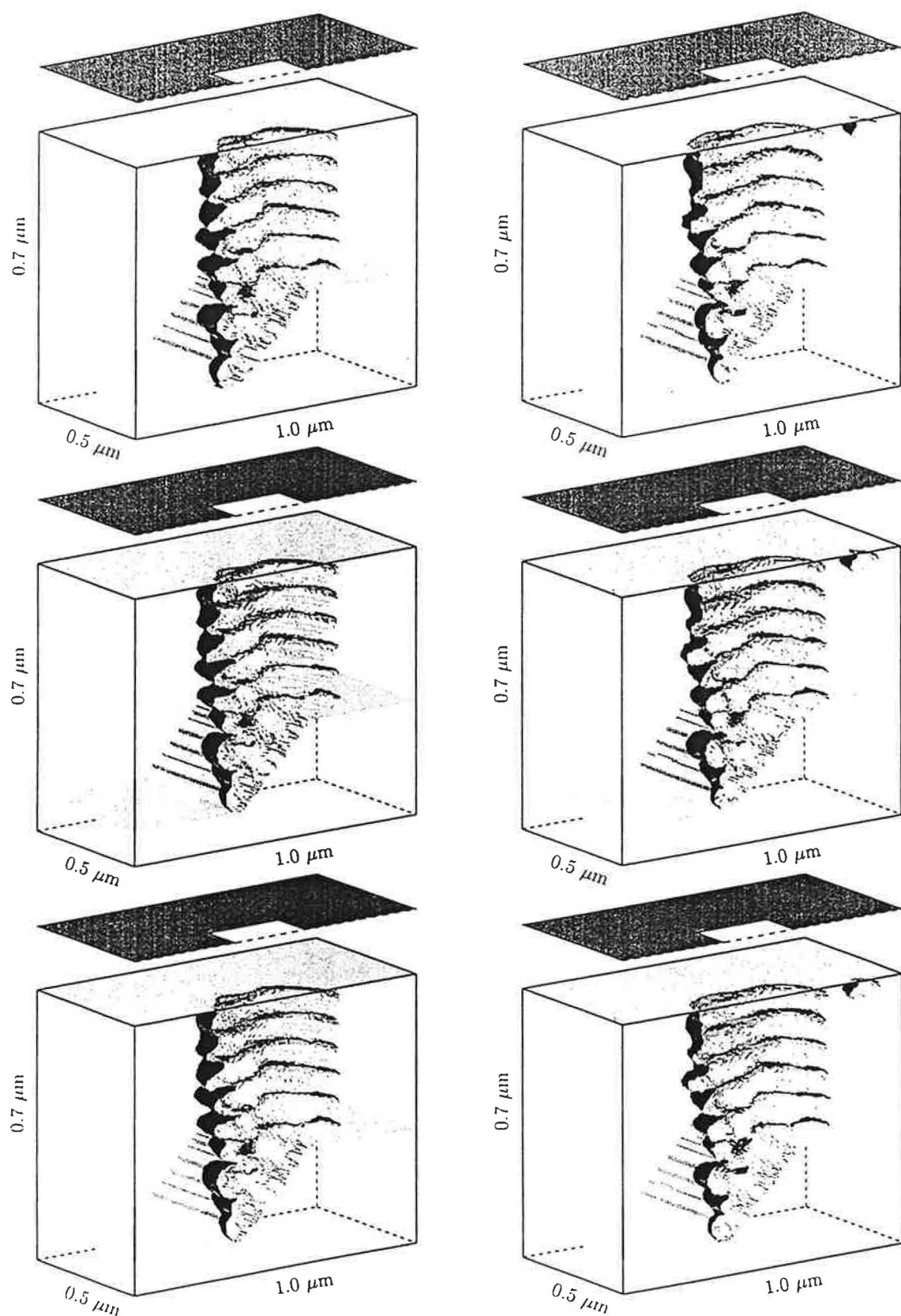
Figure 6. Resist profiles after development over a reflective a-silicon step (left: best focus, right: 1 μm defocus above; top: coherent, middle: circular, bottom: quadrupole).